

# HI HOD. I. The Halo Occupation Distribution of HI Galaxies

Fei Qin<sup>1</sup> , Cullan Howlett<sup>2</sup> , Adam R. H. Stevens<sup>3</sup> , and David Parkinson<sup>1</sup> 

<sup>1</sup> Korea Astronomy and Space Science Institute, Yuseong-gu, Daejeon 34055, Republic of Korea; [feiqin@kasi.re.kr](mailto:feiqin@kasi.re.kr)

<sup>2</sup> School of Mathematics and Physics, The University of Queensland, Brisbane, QLD 4072, Australia

<sup>3</sup> International Centre for Radio Astronomy Research, The University of Western Australia, Crawley, WA 6009, Australia

Received 2022 May 11; revised 2022 July 22; accepted 2022 August 20; published 2022 October 4

## Abstract

The next generation of galaxy surveys will provide more precise measurements of galaxy clustering than have previously been possible. The 21 cm radio signals that are emitted from neutral atomic hydrogen (HI) gas will be detected by large-area radio surveys such as the Widefield Australian Square Kilometre Array (SKA) Pathfinder L-band Legacy All-sky Blind Survey and SKA, and deliver galaxy positions and velocities that can be used to measure galaxy clustering statistics. However, to harness this information to improve our cosmological understanding and learn about the physics of dark matter and dark energy, we need to accurately model the manner in which galaxies detected in HI trace the underlying matter distribution of the universe. For this purpose, we develop a new HI-based halo occupation distribution (HOD) model, which makes predictions for the number of galaxies present in dark matter halos conditional on their HI mass. The parameterized HOD model is fit and validated using the DARK SAGE semi-analytic model, where we show that the HOD parameters can be modeled by simple linear and quadratic functions of the HI mass. However, we also find that the clustering predicted by the HOD depends sensitively on the radial distributions of the HI galaxies within their host dark matter halos, which does not follow the Navarro–Frenk–White profile in the DARK SAGE simulation. As such, this work enables—for the first time—a simple prescription for placing galaxies of different HI masses within dark matter halos in a way that is able to reproduce the HI mass-dependent galaxy clustering and HI mass function simultaneously and without requiring knowledge of the optical properties of the galaxies. Further efforts are required to demonstrate that this model can be used to produce large ensembles of mock galaxy catalogs for upcoming surveys.

*Unified Astronomy Thesaurus concepts:* [Cosmology \(343\)](#); [Large-scale structure of the universe \(902\)](#); [Galaxy dark matter halos \(1880\)](#)

## 1. Introduction

The large-scale structure of matter in the universe, as traced out by the distribution of galaxies and light, provides an important observational probe of the physics of the origin and evolution of the universe. The clustering statistics of the three-dimensional galaxy distribution can be used to measure the expansion rate of the universe (through baryon acoustic oscillations) and the rate at which structures form (using redshift-space distortions and peculiar velocities). These cosmological probes have already been used as powerful tools to test the standard cosmological model of  $\Lambda$  cold dark matter ( $\Lambda$ CDM) and constrain the parameters relating to dark matter and dark energy (Gorski et al. 1989; Feldman et al. 1994; Hatton & Cole 1998; Cole et al. 2005; Yamamoto et al. 2006; Beutler et al. 2012; Johnson et al. 2014; Carrick et al. 2015; Blake et al. 2018; Shi et al. 2018; Dupuy et al. 2019; Howlett 2019; Qin et al. 2019a, 2019b). As the next generation of surveys increase in depth, volume, and population number, these cosmological measurements will only increase in precision.

However, guaranteeing the accuracy of such clustering measurements requires detailed modeling of the galaxy survey. Accurate cosmological inferences need to include the manner in which the observed “tracer galaxies” map the underlying dark matter distribution, the effects of the survey selection function, geometry and completeness, and the possible

ensemble of clustering measurements (of which our universe is only a single realization) known as cosmic variance.

These effects are most commonly accounted for using large ensembles of numerical simulations, for example, the WIZCOLA (Koda et al. 2016), L-PICOLA (Howlett et al. 2015b), Quijote (Villaescusa-Navarro et al. 2020), or AbacusSummit (Maksimova et al. 2021) simulation suites. A popular method for then populating these simulations with galaxies is the halo occupation distribution (HOD; Jing et al. 1998; Peacock & Smith 2000; Berlind & Weinberg 2002; Zheng 2004; Tinker et al. 2005; Guo et al. 2013, and references therein). These methods do not track the formation of a galaxy from gas in the simulation directly. Instead the HOD is a statistical approach, using an empirical relationship between the dark matter halo mass and the probability of finding galaxies in that halo at a given position or with certain properties. This semi-empirical relationship comes from either simulations that involve galaxy formation, or else from existing data sets.

If one can directly use galaxy formation theory and simulations to generate fake galaxies and fake surveys, why use the HOD approach? This is mainly due to the fact that it is slower to generate galaxies using galaxy formation theory, and robust and accurate dark matter halo properties and merger trees are required. For the large ensembles of simulations required to estimate the variance in clustering measurements, the mass resolution is typically limited, and the halo properties are often only reproduced approximately (see, e.g., Manera et al. 2015; Howlett et al. 2015b; Blot et al. 2019). However, using an HOD, one can quickly generate a large number, usually thousands, of mock galaxy surveys and compensate for



Original content from this work may be used under the terms of the [Creative Commons Attribution 4.0 licence](#). Any further distribution of this work must maintain attribution to the author(s) and the title of the work, journal citation and DOI.

the lack of fidelity in the underlying dark matter and halo clustering.

To date, most cosmological measurements from galaxy surveys have relied on optical redshifts to map the large-scale structure in our universe. However, in the coming years, we will start to see the advent of large-scale radio surveys being used for precision cosmology. For example the Widefield Australian Square Kilometre Array Pathfinder (ASKAP) L-band Legacy All-sky Blind surveY (WALLABY; Koribalski et al. 2020) and the Square Kilometre Array (SKA; Square Kilometre Array Cosmology Science Working Group et al. 2020) will provide a large number of late-type galaxies with observed redshifts, and distances measured using the Tully–Fisher relation (which is the empirical relation between a galaxy’s absolute magnitude and its H I rotation width; Tully & Fisher 1977; Strauss & Willick 1995; Masters et al. 2008; Hong et al. 2019; Kourkchi et al. 2020). To harness those surveys for cosmology, we need to understand how galaxies detected in H I trace the underlying matter distribution of the universe. This essentially demands the development of an HOD conditional on the H I mass. This is important, as not every 21 cm galaxy (or H I-emitting object) will populate the dark matter halo in the same way, regardless of mass. Instead the relationship between H I mass and dark matter halo mass will be complicated by astrophysical effects during galaxy formation. An H I-conditional HOD allows us to build up a realistic model of the radio galaxy distribution, not just by position on the sky, but also by H I mass. This is analogous to other work that has focused on conditional luminosity and stellar mass functions (e.g., Cooray 2006; Guo et al. 2018).

The relation between H I mass and dark matter halo mass has been explored in many previous works (Padmanabhan et al. 2017; Castorina & Villaescusa-Navarro 2017; Villaescusa-Navarro et al. 2018; Obuljen et al. 2019; Guo et al. 2020; Chauhan et al. 2020; Avila et al. 2022). For example, Obuljen et al. (2019) and Guo et al. (2020) constrain the parameters in the H I halo mass relation using the ALFALFA survey (Giovanelli et al. 2005). Chauhan et al. (2020) studied the H I halo mass relation using the semi-analytic galaxy formation model SHARK (Lagos et al. 2018a, 2018b), where they explore the effect of different physical processes on the shape of the H I halo mass relation. However, these cases have only explored one aspect of the problem at a time: either considering the total H I mass in a given halo, or the number of H I galaxies across a survey (perhaps as a function of the environment but largely irrespective of the halo mass). Paranjape et al. (2021a) and Paranjape et al. (2021b) use an optical HOD of Guo et al. (2015b) and scaling relation of Paul et al. (2018) to predict the clustering of H I selected galaxies in different H I mass bins, assuming the optical and H I selected galaxies statistically trace out the same underlying halo distribution. However, this requires knowledge of the optical properties of the galaxies.

In this work, we model both aspects simultaneously and without requiring knowledge of the optical properties of the galaxies, and develop a methodology for producing simulations for 21 cm radio galaxy (hereafter, H I galaxy) surveys such as the WALLABY and SKA, which will measure the galaxy position and redshift through neutral hydrogen emission. In this first paper, we develop an improved conditional HOD model; in later work we will demonstrate how this can be painted onto approximate simulations before applying survey selection effects.

The paper is structured as follows: In Section 2, we introduce the DARK SAGE simulation, which will be used to explore the connection between H I mass, halo mass, and galaxy clustering. In Section 3, we introduce the H I-mass-conditional HOD that we will be fitting. In Section 4, we introduce the galaxy two-point correlation function, and the halo properties that are used to model it. In Sections 5 and 6, we apply this modeling to the DARK SAGE simulation, showing how the parameters of the model can be fit first from the galaxy distribution as a function of the halo mass and then from only the galaxy clustering. We conclude in Section 7. Hereafter, the little letter  $m$  denotes the mass in the real space, while the capital letter  $M \equiv \log_{10} m/m_{\odot}$  denotes the mass in the log-space per unit solar mass  $m_{\odot}$ .

## 2. The Dark Sage Model

In this work we use a simulated catalog of galaxies to fit an H I-based HOD that is conditional on the H I mass (i.e., it makes different predictions for the halo distribution of that object based on its neutral hydrogen mass). This simulated catalog is built from the DARK SAGE semi-analytic model of galaxy formation, specifically the version of Stevens et al. (2018).

Originally presented in Stevens et al. (2016)—with updates in Stevens & Brown (2017) and Stevens et al. (2018)—DARK SAGE builds and evolves galaxies within halo merger trees constructed from a cosmological  $N$ -body simulation. The version used here was run on the standard merger trees of the Millennium simulation (Springel et al. 2005), widely used throughout the literature. This simulation assumes a  $\Lambda$ CDM cosmology with parameters based on the WMAP1 best-fit cosmology (Spergel et al. 2003):  $\sigma_8 = 0.9$ ,  $n_s = 1$ ,  $\Omega_m = 0.25$ ,  $\Omega_b = 0.045$ ,  $\Omega_{\Lambda} = 0.75$ , and  $h = 0.73$  (where  $H_0 = 100 h \text{ km s}^{-1} \text{ Mpc}^{-1}$ ). Millennium has a comoving box size of  $500 h^{-1} \text{ Mpc}$  with  $2160^3$  particles of mass  $8.6 \times 10^8 h^{-1} \text{ m}_{\odot}$ . The minimum mass for a (sub)halo in the merger trees is 20 times the particle mass.

DARK SAGE belongs to the SAGE (Semi-Analytic Galaxy Evolution) family of models, building on Croton et al. (2016), but with the addition of many novel features. Where classical semi-analytic models describe the stellar and gas disks of galaxies each with a singular reservoir with an analytic density profile, disks in DARK SAGE are instead split into 30 annuli, allowing the density profile of the galaxy to be built numerically. The model accounts for what is understood to be the core astrophysical processes relevant to galaxy evolution: gas cooling and accretion, star formation and stellar feedback, central black hole growth and associated feedback from active galactic nuclei, gravitational disk instabilities, galaxy mergers, and environmental stripping of gas. Within each disk annulus, gas is broken into its ionized, atomic, and molecular phases (based on McKee & Krumholz 2010; Fu et al. 2013). Star formation, stellar feedback, and disk instabilities all take place locally, affecting the structure of the gas disk and therefore its overall H I content (of central relevance to this work).

The eight free parameters of this version of DARK SAGE were manually calibrated to reproduce a set of observables. Most notably for this work, these include the H I mass function (based on data from Zwaan et al. 2005; Martin et al. 2010), the stellar mass function (Baldry et al. 2008), and the mean H I-to-stellar mass ratio of galaxies as a function of the stellar mass (Brown et al. 2015; all three of

these are at  $z \simeq 0$ ). Further details can be found in Appendix B of Stevens et al. (2018).

To minimize our results from being biased by unresolved systems in our sample, we exclude galaxies from our DARK SAGE catalog that reside in (sub)halos with a maximum historical mass<sup>4</sup> less than the equivalent of 100 particles ( $8.6 \times 10^{10} h^{-1} m_{\odot}$ ), in line with Onions et al. (2012). These systems are excluded in all parts of this paper, including where we present (sub)halo-specific results in Section 4. Given this halo mass limit, we argue that galaxies with an H I mass above  $10^9 h^{-1} m_{\odot}$  are those that are sufficiently complete in terms of the halo mass and therefore trustworthy for the purposes of this work. We expect galaxies above these masses to be the most relevant for clustering (as they can be detected to greater distances, and hence increase the cosmological volume and clustering signal-to-noise) and Tully–Fisher measurements (as they are the highest signal-to-noise objects with the best measured rotation measurements). For example, this limit is below the mean and peak H I masses of objects detected in the WALLABY pilot surveys.

Although the version of DARK SAGE we are using here is built on a relatively old  $N$ -body simulation (Millennium), we use this as it is well tested and characterized in the literature (Stevens et al. 2018, 2019a), which makes for easier understanding of the analytic models we develop here. As the aim of this work is to set up the first stages for a flexible H I-based HOD, we do not think it is particularly important which simulation is used here and defer a detailed look at the impact of different simulations and simulation choices for later work.

### 3. The H I-mass-conditional HOD

#### 3.1. The Standard Halo Occupation Distribution Model

The standard HOD model contains the following three aspects: (1) the number of galaxies in a parent halo; (2) the spatial distribution of the galaxies in their parent halo; (3) the velocities of these galaxies. The last two aspects are modeled by the halo density profile, for example, the Navarro–Frenk–White (NFW) profile (Navarro et al. 1996, 1997). While the first aspect, that is, predicting how many galaxies are in a parent halo is the main goal of the study of HOD, and therefore is what the term HOD commonly refers to.

Let  $f_h(M)dM$  denote the number of parent halos in an infinitesimally small halo mass bin  $[M, M + dM]$ , where  $M$  denotes (log) halo mass,  $f_h(M)$  is the halo mass function, which has been well characterized from simulations (i.e., Jenkins et al. 2001; Tinker et al. 2005), but which for now we leave unspecified. If there are  $dn_c$  central galaxies in these  $f_h(M)dM$  parent halos and  $dn_s$  satellite galaxies, the HOD of central and satellite galaxies of that halo mass bin are defined as

$$\langle N_{\text{cen}}(M) \rangle \equiv \frac{dn_c}{f_h(M)dM}, \quad (1a)$$

$$\langle N_{\text{sat}}(M) \rangle \equiv \frac{dn_s}{f_h(M)dM}, \quad (1b)$$

respectively. The physical meaning of the HOD is that if the mass of a parent halo is  $M$ , the probability that it hosts a central galaxy is  $\langle N_{\text{cen}}(M) \rangle$  of Equation (1a), while the probability that

<sup>4</sup> The “maximum historical mass” is the greatest mass of the (sub)halo found from walking back in time along the primary-progenitor branch of that subhalo in its merger tree of the Millennium simulation.

it hosts a satellite galaxy is  $\langle N_{\text{sat}}(M) \rangle$  of Equation (1b). A parent halo can host only one central galaxy at most but multiple satellite galaxies, typically increasing in number with the halo mass.

There are several commonly used HOD models in past works. Berlind & Weinberg (2002) model  $\langle N_{\text{sat}} \rangle$  using a simple power-law function and assuming  $\langle N_{\text{cen}} \rangle = 1$ , that is, each parent halo hosts one central galaxy. Tinker et al. (2005) models  $\langle N_{\text{sat}} \rangle$  using an exponential function multiplied by a power-law function while retaining  $\langle N_{\text{cen}} \rangle = 1$ . Zheng et al. (2007) models  $\langle N_{\text{cen}} \rangle$  using the error function while modeling  $\langle N_{\text{sat}} \rangle$  using a power-law function multiplied by the error function. This model has been commonly used in previous research (Guo et al. 2014, 2015a; Manera et al. 2015; Howlett et al. 2015b) to generate mock galaxy surveys.

These commonly used HOD models have been shown to work poorly for H I (Calette et al. 2021; Chauhan et al. 2021; Hadzhiyska et al. 2021) or more complex types of galaxies, such as emission-line galaxies (Gonzalez-Perez et al. 2018; Avila et al. 2020). Therefore, in this paper, we develop a new HOD model that adds another dimension to the standard HOD, based on the predictions of the DARK SAGE simulation.

#### 3.2. The Definition of the H I-mass-conditional HOD

We can expand our definitions of  $\langle N_{\text{cen}} \rangle$  and  $\langle N_{\text{sat}} \rangle$  to represent the probability of a halo to host a central or satellite galaxy of a given H I mass using

$$\langle N_{\text{cen}}(M, M_{\text{HI}}) \rangle \equiv \frac{dn_{c,\text{HI}}}{f_h(M)\varphi(M_{\text{HI}})dM dM_{\text{HI}}}, \quad (2a)$$

$$\langle N_{\text{sat}}(M, M_{\text{HI}}) \rangle \equiv \frac{dn_{s,\text{HI}}}{f_h(M)\varphi(M_{\text{HI}})dM dM_{\text{HI}}}, \quad (2b)$$

where  $dn_{c,\text{HI}}$  and  $dn_{s,\text{HI}}$  denote the number of galaxies in an infinitesimally small two-dimensional bin bounded by  $[M, M + dM]$  and  $[M_{\text{HI}}, M_{\text{HI}} + dM_{\text{HI}}]$ .  $\varphi(M_{\text{HI}})$  denotes the H I mass function (Zwaan et al. 2003, 2005; Jones et al. 2018).

Defined in this way, the H I-conditional HOD reduces down to the standard HOD defined in Equation (1a) through integration over H I mass. Similar integration over the halo mass returns the H I mass function, and integrating over both simply returns the total number of galaxies in the sample.

The top two panels of Figure 1 display the HOD of H I galaxies measured from the DARK SAGE simulation. The top panel shows the HOD of the central galaxies, and the middle panel shows the HOD of the satellite galaxies. The colors of the curves indicate the H I mass of the galaxies, based on the histogram of the bottom panel. In this sense, Figure 1 is effectively a normalized 2D histogram across H I and the halo mass (split additionally into central and satellite populations) measured directly from DARK SAGE.

The histogram in the bottom panel of Figure 1 only displays the distribution of H I mass above  $10^9 h^{-1} m_{\odot}$ , which is the effective resolution limit of our DARK SAGE catalog. As a result of this resolution limit, the sum of  $\langle N_{\text{cen}}(M, M_{\text{HI}}) \rangle$  over all H I mass bins we consider is less than 1, even though every halo used in DARK SAGE is assigned a central galaxy. We confirmed that including H I mass bins lower than  $10^9 h^{-1} m_{\odot}$  recovers a total number of central galaxies equal to the number of halos, but do not enforce this condition or use such low H I

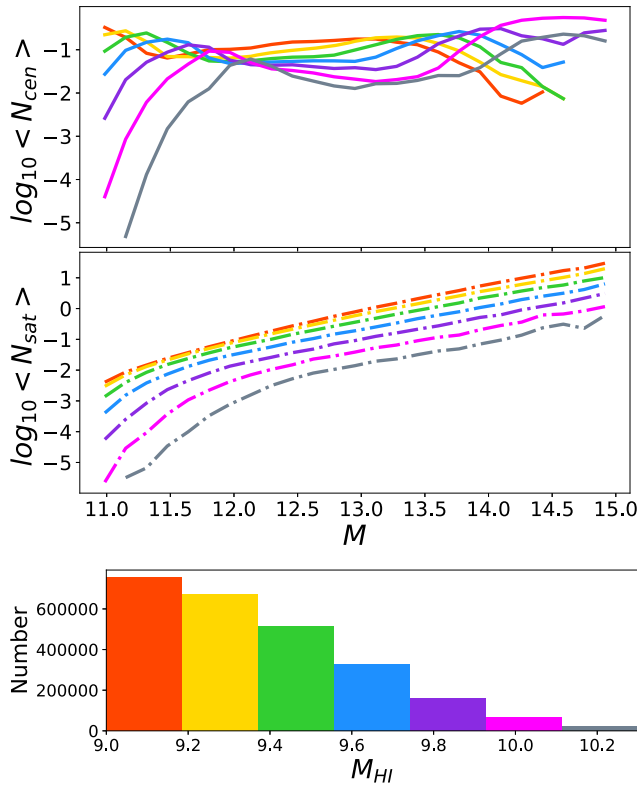


**Figure 1.** HOD of H I galaxies as measured from the output of DARK SAGE. The top panel showcases the HOD of central galaxies: that is, the probability that a halo of a given mass (per the x-axis) will host a central galaxy of a given H I mass. The middle panel showcases the HOD of satellite galaxies: that is, the expected number of satellites within a given H I mass bin to exist in a halo of a given mass. The color of the curves in the top and middle panels indicate the H I mass of the galaxies, corresponding to the bar of the same color in the bottom panel.

mass bins in the remainder of our analysis as their clustering and distribution is less reliable.

### 3.3. The H I-mass-conditional HOD Model

From the top panel of Figure 1, we find that the HOD measured from the central galaxies showcases a characteristic “M” shape as a function of the halo mass, but with a position and size of “dip” that depends on the H I mass we consider. In intermediate-mass halos, namely, around  $11.8 < M < 13.5$ , this is caused by active galactic nuclei feedback “turning on”, which slows down the gas cooling and hence the replenishment of H I gas within central galaxies (see Section 4.1.1 of Chauhan et al. 2020 for further discussion). Therefore the HOD of central galaxies is mildly decreased in this region. In low-mass halos the number of high-H I-mass centrals decreases rapidly as the H I mass approaches a significant fraction of the halo mass, due to the inability of these halos to retain and cool the gas.

The HOD for satellites follows a more usual power-law shape, with high-mass halos hosting more satellites, but again with an exponential decline toward lower halo masses due to the relative inability of galaxies in these halos to retain, accrete, and cool new material. The amplitude of the satellite HOD increases with decreasing H I mass—to be expected given the shape of the H I mass function and relative abundances of low versus high-H I-mass galaxies; however, there is also evidence

that higher-H I-mass satellites experience a stronger exponential decrease in their abundance as we go to lower halo masses.

To model the HOD of the central and satellite galaxies, we take inspiration from Weigel et al. (2016), using double and single Schechter functions for the central and satellite HODs, respectively:

$$\langle N_{\text{cen}}(M, M_{\text{HI}}) \rangle = \phi_c 10^{\beta_1(M_c - M)} \exp[-10^{(M_c - M)}] + \phi_a 10^{\beta_2(M - M_a)} \exp[-10^{(M - M_a)}], \quad (3a)$$

$$\langle N_{\text{sat}}(M, M_{\text{HI}}) \rangle = \phi_s 10^{\beta_s(M_s - M)} \exp[-10^{(M_s - M)}], \quad (3b)$$

where parameters  $M_c$ ,  $\beta_1$ ,  $\beta_2$ ,  $\phi_c$ ,  $\phi_a$ ,  $M_a$  and  $M_s$ ,  $\beta_s$ ,  $\phi_s$  are functions of the H I mass. However, as we show in Section 6.2 there can be strong correlations between these parameters that allow us to reduce the model dimensionality. They can be fitted from the measured HOD or the galaxy two-point correlation function. How this can be done is the subject of the next section.

## 4. The Correlation Function and the Halo Distribution

In this section we show how the HOD can be fit by comparing a model galaxy two-point correlation function to the measured correlation function of a real galaxy survey.<sup>5</sup> To achieve this goal, we need to first write down the model galaxy two-point correlation function in terms of the HOD, then compare the model to the measurement to determine the HOD parameters.

The galaxy two-point correlation function can be decomposed into the sum of a “one-halo” term,  $\xi_{gg}^{1h}$ , and a “two-halo” term,  $\xi_{gg}^{2h}$ , written as (Berlind & Weinberg 2002; Yang et al. 2003; Zheng 2004)

$$\xi_{gg}(r) = [1 + \xi_{gg}^{1h}(r)] + \xi_{gg}^{2h}(r), \quad (4)$$

where  $r$  is the pair separation. The one-halo term is the contribution from intrahalo pairs: that is, two satellites, or one central and one satellite, situated within the same halo. The two-halo term is the contribution from intrahalo pairs: that is, two galaxies, centrals or satellites, in their own unique halos.

### 4.1. The One-halo Term

The model of the one-halo term can be expressed as (Berlind & Weinberg 2002; Tinker et al. 2005; Zheng & Guo 2016)

$$1 + \xi_{gg}^{1h}(r) = \frac{1}{2\pi r^2 \bar{n}_g^2} \int_0^\infty \frac{1}{\alpha R_{\text{vir}}} [\langle N_{\text{cen}} N_{\text{sat}} \rangle f_{cs}(x) + \frac{\langle N_{\text{sat}}(N_{\text{sat}} - 1) \rangle}{2} f_{ss}(x)] f_h(m) dm, \quad (5)$$

where  $x \equiv \frac{r}{\alpha R_{\text{vir}}}$ ,  $f_h(m)$  is the halo mass function,  $\bar{n}_g$  is the average number density of galaxies.  $\alpha$  is a parameter chosen to set the maximum extent of what we consider to be within “one halo”. We also assume that the number of galaxies follows the Poisson distribution,  $\langle N_{\text{sat}}(N_{\text{sat}} - 1) \rangle = \langle N_{\text{sat}} \rangle^2$  (Berlind & Weinberg 2002; Tinker et al. 2005).  $\bar{n}_g$  can be calculated

<sup>5</sup> In this paper, the “real galaxy survey” has been replaced with a simulated data set from a semi-analytic model, but we expect the methodology to remain valid.

using (Yang et al. 2003; Tinker et al. 2005)

$$\bar{n}_g = \int_0^\infty [\langle N_{\text{cen}} \rangle + \langle N_{\text{sat}} \rangle] f_h(m) dm. \quad (6)$$

For the DARK SAGE simulation,  $\bar{n}_g$  can also be simply calculated using  $\bar{n}_g = N_g/V$ , where  $N_g$  is the total number of galaxies in the simulation, and  $V$  is the volume of the simulation box.

The virial radius of a halo,  $R_{\text{vir}}$  is computed from the halo mass using

$$R_{\text{vir}} = \left( \frac{3m}{4\pi\Delta\rho_c} \right)^{1/3}, \quad (7)$$

where  $\Delta = 200$  is the overdensity threshold of halo identification, consistent with the definition of the halo (virial) mass in the simulation.  $\rho_c = 3H_0^2/(8\pi G)$  is the critical density of the (simulated) universe, where  $G$  is Newton’s gravitational constant and  $H_0$  the Hubble constant.

$f_{\text{cs}}(x)$  expresses the radial distribution of central–satellite galaxy pairs in a parent halo (Zheng 2004; Tinker et al. 2005; Zheng & Weinberg 2007), which, as the central galaxy is presumed to sit in the center of mass of the halo, is usually written in terms of the halo radial density profile  $\rho_m(r)$

$$f_{\text{cs}}(x) \propto \rho_m(r) r^2. \quad (8)$$

$f_{\text{ss}}(x)$  is the probability density function (PDF) of satellite galaxy pairs in a parent halo. This is more difficult to express and requires convolving a given halo density profile with itself. It can be done analytically for the truncated NFW density profile (and others; see Appendix A of Zheng & Weinberg 2007) although the resulting expressions are cumbersome and so not repeated here. As PDFs, both  $f_{\text{cs}}(x)$  and  $f_{\text{ss}}(x)$  should be normalized to 1 when integrating from  $x = 0$  to  $x = 1$  (Zheng 2004; Tinker et al. 2005; Zheng & Weinberg 2007; Zheng & Guo 2016).

It is important to note that Equation (5) is general and can apply for any radial distribution or (radially symmetric) halo profile. However, the commonly used forms for  $f_{\text{cs}}(x)$  and  $f_{\text{ss}}(x)$  are for the distribution of dark matter within halos. As we are interested in the galaxy correlation function, these may not be appropriate to use if the distribution of galaxies differs significantly from the dark matter. We investigate this for our simulated H I galaxies in Section 5.

#### 4.2. The Two-halo Term

The two-halo term  $\xi_{gg}^{2h}(r)$  is the contribution from intrahalo galaxy pairs. The basic assumption behind this term is that the clustering of galaxies can be written in terms of the underlying matter clustering multiplied by the galaxy bias,  $b_g(k)$ , which here is written as a function of the Fourier scale  $k$ . The galaxy bias then stems from the underlying halo bias function  $b_h(m)$ , weighted by the occupancy of each halo, and the (Fourier-space) halo density profile (Berlind & Weinberg 2002).

However, following the arguments in Zheng (2004), at any given separation it is important to only include galaxy pairs arising from two different distinct halos. At separations within the transition region from the one- to two-halo terms it becomes important to consider that *two* halos simply may not exist—their extent is such that they would have merged to form a single larger halo. This concept, called “halo exclusion”, can be incorporated into the model by requiring that the pair

separation  $r$  must be larger than double the halo’s virial radius, that is,  $r > 2R_{\text{vir}}$ . Using Equation (7), one can then find the following mass limit (Zheng 2004; Tinker et al. 2005)

$$m_{\text{lim}}(r) = \frac{4}{3}\pi\left(\frac{r}{2}\right)^3\rho_c\Delta, \quad (9)$$

which can be used to enforce that only if the halo mass  $m$  is less than  $m_{\text{lim}}(r)$ , should it be included into the two-halo term for pair separation  $r$ .

From these considerations, the model of the two-halo term  $\xi_{gg}^{2h}(r)$  is given by Zheng (2004), Tinker et al. (2005), and Zheng & Weinberg (2007)

$$\xi_{gg}^{2h}(r) = [1 + \xi'_{2h}(r)]\left(\frac{\bar{n}'_g}{\bar{n}_g}\right)^2 - 1, \quad (10)$$

where

$$\bar{n}'_g = \int_0^{m_{\text{lim}}(r)} [\langle N_{\text{cen}} \rangle + \langle N_{\text{sat}} \rangle] f_h(m) dm, \quad (11)$$

is the average number density of galaxies that reside in halos with  $m \leq m_{\text{lim}}$ . The unnormalized correlation function,  $\xi'_{2h}(r)$ , is computed by inverse Fourier transforming the galaxy power spectrum, such that

$$\xi'_{2h}(r) = \frac{1}{2\pi^2} \int_0^\infty b_g^2(k, r) P_m(k) k^2 \frac{\sin(kr)}{kr} dk, \quad (12)$$

where  $P_m(k)$  is the nonlinear matter power spectrum (which we generate using the CAMB package; Lewis et al. 2000; Howlett et al. 2012). The galaxy biasing parameter  $b_g$  is given by

$$b_g = \frac{1}{\bar{n}'_g} \int_0^{m_{\text{lim}}(r)} [\langle N_{\text{cen}} \rangle + \langle N_{\text{sat}} \rangle] b_h(m) y_g(k) f_h(m) dm, \quad (13)$$

where  $b_h(m)$  is the halo biasing parameter; see Appendix A.  $y_g(k)$  is the Fourier transformation of  $\rho_m$  of Equation (8), defined as (Cooray & Sheth 2002)

$$y_g(k) \equiv \int_0^{R_{\text{vir}}} 4\pi R^2 \frac{\sin(kR)}{kR} \frac{\rho_m(R)}{m} dR. \quad (14)$$

Assuming the galaxies follow the NFW profile,  $y_g$  is given by Equation (B4).

The model described above is perhaps the simplest model one can consider that incorporates halo exclusion. However, it does not account for the cross correlation between two halos where only one has mass less than  $m_{\text{lim}}$ . It also does not account for the ellipsoidal nature of halos. Tinker et al. (2005) discuss both of these issues and explore more sophisticated treatments that can account for them. However, for this first work we consider the simpler and less computationally intensive model.

In the next section, we use our model for the correlation function to fit for the HOD parameters in the DARK SAGE simulation. We also explore some of the assumptions in the modeling, particularly the intrahalo distributions of H I galaxies, and characterize how well they represent our simulation.

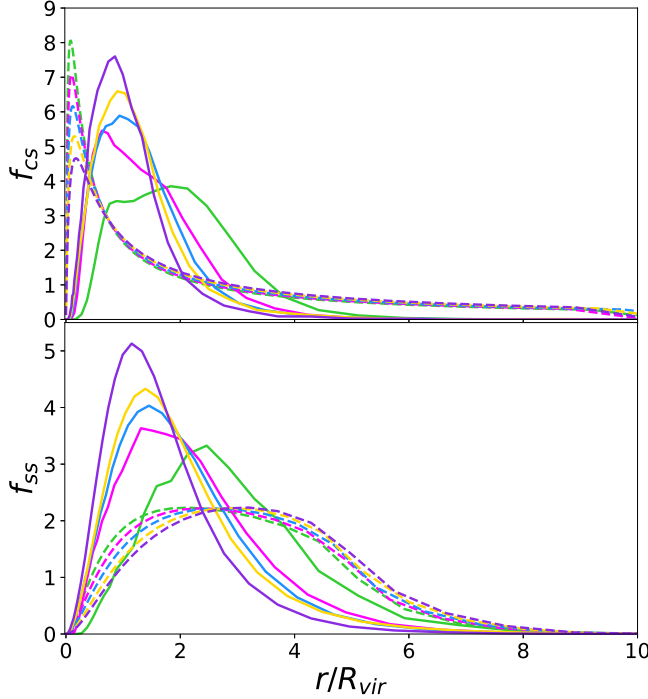


**Figure 2.** The  $f_{\text{cs}}$  and  $f_{\text{ss}}$  for five example halo mass bins. The green, pink, blue, yellow, and purple colored lines are for halo mass bins centered on  $M = 11.31, 12.13, 12.95, 13.77$ , and  $14.59$ , respectively. The dashed curves depict the NFW profile for these masses. The solid curves showcase the measurements from DARK SAGE. All these curves (both solid and dashed) are normalized to integrate to one in the interval  $x \in [0, 1]$ .

## 5. Application to the Full DARK SAGE Simulation

### 5.1. Validating the Radial Profiles

We begin by measuring the basic ingredients going into our model of the correlation function, the  $f_{\text{cs}}$ ,  $f_{\text{ss}}$ , and  $y_g$  profiles of the HI galaxies in the DARK SAGE simulation; then we compare them to the NFW halo density profile.

$f_{\text{cs}}$  and  $f_{\text{ss}}$  are computed by splitting the halos into five different mass bins in the interval  $M \in [10.9, 15]$  and counting the number of central–satellite and satellite–satellite pairs in these halos. We plot them against  $r/R_{\text{vir}}$  in Figure 2, normalized to integrate to one in the interval  $x \in [0, 1]$  with  $\alpha = 10$ . The  $f_{\text{cs}}$  and  $f_{\text{ss}}$  curves derived from the NFW profile are also shown in the figure with the same normalization. As can be seen, there is poor agreement between the measurements of the pairwise distributions of the HI galaxies (which directly traces the distribution of resolved subhalos in the Millennium simulation) from DARK SAGE and an NFW profile, even if we allow for galaxies separated as far apart as  $10 R_{\text{vir}}$  (where, typically, one would invoke an upper limit of  $2 R_{\text{vir}}$ ).

Clearly, Millennium subhalos (and therefore DARK SAGE satellite galaxies) are mostly found at separations from their central around or beyond the virial radius of the halo. A “halo” from the perspective of the framework we are using here is just a friends-of-friends group of particles (Springel et al. 2005). This has a calculable  $R_{\text{vir}}$ , but the group itself can extend well beyond the virial radius. The peak distance for subhalos is around  $R_{\text{vir}}$  because close to the halo center, subhalos can merge with the central, get disrupted, or become harder to identify, which can result in their removal from the merger trees used as an input for a semi-analytic model (see, e.g., Onions et al. 2012; Poulton et al. 2020).

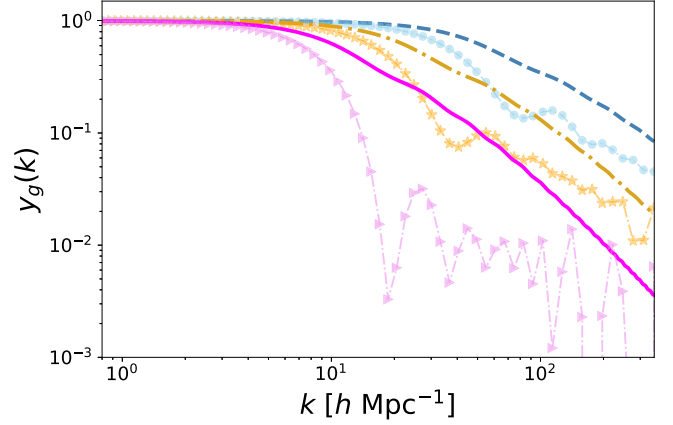


**Figure 3.** The dashed, dashed-dotted, and solid curves depict the Fourier transformation of the NFW profile calculated using Equation (B4). The dots, stars, and triangular markers showcase the Fourier transformation of the measured galaxy radial distribution from the DARK SAGE simulation. The blue color is for halo mass  $M = 11$ , the brown color is for halo mass  $M = 12$ , and the pink color is for halo mass  $M = 13$ .

It is also important to note that part of the reason why there are fewer satellite galaxies closer to halo centers in DARK SAGE is also because there are no “orphan” galaxies (that is, galaxies that have lost their dark matter subhalo). For an HI study, the lack of orphans is less of a cause for concern than it would be for an optical study, because if a subhalo is tidally stripped to the point that it is no longer resolvable in the  $N$ -body simulation, then the gas in that subhalo’s galaxy would also be quite susceptible to stripping processes too (see the clustering results of Knebe et al. 2018). Hence, we are making the implicit, but physically reasonable, assumption in this study that galaxies without appreciable dark matter also lack appreciable gas through tidal forces and ram pressure stripping.

A secondary trend can also be seen in Figure 2, where lower-mass halos typically host satellites at larger distances. This is because the merger timescales are shorter for low-mass halos, where the masses of the merging systems should statistically be more comparable. High-mass halos can host satellites stably orbiting at a range of distances because the satellites are often relatively small, to the point that they have next to no gravitational influence on the rest of the halo.

As a result, it is clear that enforcing all HI galaxies to be within  $2R_{\text{vir}}$  and to follow  $f_{\text{cs}}$  and  $f_{\text{ss}}$  derived from an NFW profile is inappropriate. We find that, to cover all the measured  $f_{\text{cs}}$  and  $f_{\text{ss}}$  curves, the normalization interval should allow for separations up to  $10R_{\text{vir}}$ . To do this, we set  $\alpha = 10$  in our model for the one-halo term of the correlation function Equation (5) going forward, and normalize the measured  $f_{\text{cs}}$  and  $f_{\text{ss}}$  of DARK SAGE simulation in  $x \in [0, 1]$ . We then use the measured curves as input for our modeling.

We also measure  $y_g$  of the HI galaxies in the DARK SAGE simulation using the same halo mass bins as above. We do this first by calculating  $\rho_g$ , the galaxy density profile, from the measured  $f_{\text{cs}}$  using Equation (8). Then we calculate  $y_g$  using Equation (14), normalizing it to 1 at  $k = 0 h \text{ Mpc}^{-1}$ . These measurements are shown in Figure 3, alongside the  $y_g(k)$  predicted from the NFW profile (calculated using Equation (B4)) for our three example halo mass values. Again, we find that the NFW profile prediction is different from the  $y_g$  measured from the DARK SAGE simulation, with less “power” on small scales (large  $k$ ). This is indicative of greater distances

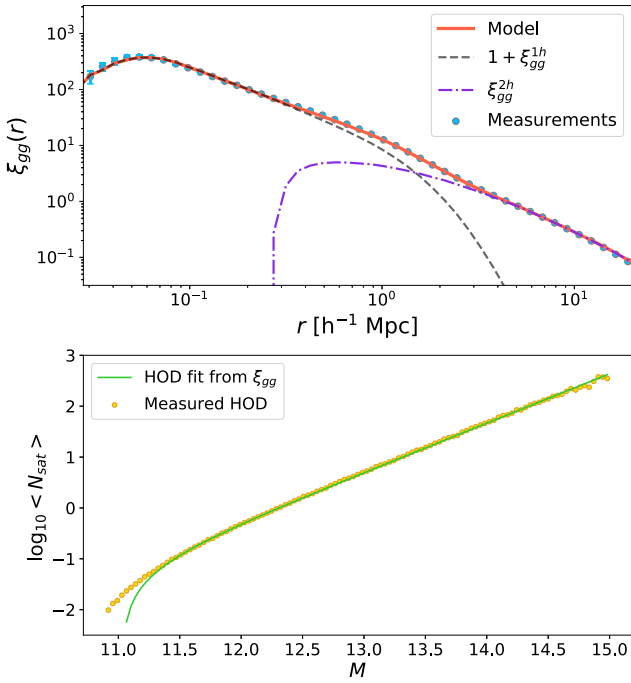


**Figure 4.** Fitted HOD parameters from the galaxy two-point correlation function for the DARK SAGE simulation. In the left-hand panels, the top shows the correlation function measurement (blue filled circles) and the model (red curve) fit to the measurement. This is further decomposed into the corresponding one-halo,  $1 + \xi_{gg}^{1h}$ , and two-halo,  $\xi_{gg}^{2h}$ , terms (dashed gray and dashed-dotted purple, respectively). The bottom panel shows the measured HOD and that inferred from the fitted correlation function (yellow points and green line, respectively). The fit results of the HOD parameters are shown in the right-hand panels. The histograms show the distribution of the MCMC samples. The shaded areas in the 1D plots indicate the 68% confidence level, while the 2D contours indicate the 1, 1.5, 2, and  $2.5\sigma$  regions.

between H I galaxies and the centers of their parent halos than would be predicted for dark matter. As such, we also use the measured values of  $y_g$  in our correlation function modeling.

Future work could aim to characterize and understand these trends in greater detail and come up with flexible functional forms that could be incorporated into the HOD modeling as required. However, for the purposes of demonstrating that it is in principle possible to model the conditional HOD of H I galaxies using the clustering, we stick with the simulation-measured distributions here.

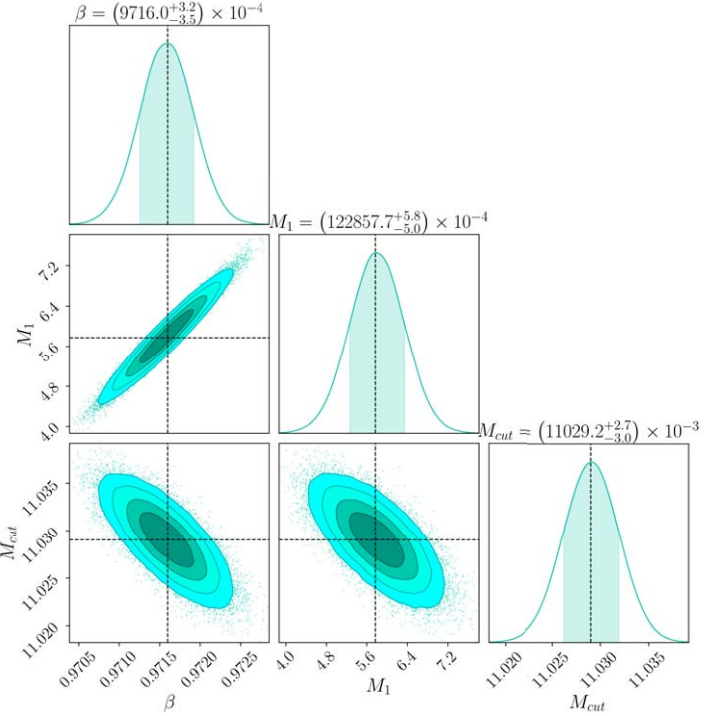
### 5.2. Fitting an HOD for the Whole DARK SAGE Simulation

In this section, we validate our fitting pipeline to show that we can fit the HOD of the whole DARK SAGE simulation *without* splitting into H I mass bins. Fits to the HOD conditional on the H I mass  $M_{\text{HI}}$  are presented later in Section 6.3.

DARK SAGE requires that each parent halo hosts a central galaxy. Therefore, the HOD of central galaxies is given by  $\langle N_{\text{cen}} \rangle = 1$ . We use the following equation to model the HOD of satellite galaxies (Zheng et al. 2007; Howlett et al. 2015b; Zheng & Guo 2016)

$$\langle N_{\text{sat}} \rangle = \langle N_{\text{cen}} \rangle \left( \frac{m - 10^{M_{\text{cut}}}}{10^{M_1}} \right)^\beta, \quad (15)$$

where parameters  $M_{\text{cut}}$ ,  $\beta$ , and  $M_1$  are the HOD parameters that need to be fit by comparing the model correlation function  $\xi_{gg}^{\text{mod}}$  of Section 4 to the measurement  $\xi_{gg}^{\text{mea}}$ .  $M_{\text{cut}}$  is the mass limit under which the halos are too small to host satellite galaxies.  $M_1$  is the amplitude of the HOD of satellite galaxies.  $\beta$



describes how fast the number of satellite galaxies increases as their parent halo mass increases; it is the slope of the HOD. Due to the fact that the galaxies in DARK SAGE do not follow the NFW profile, we use the measured  $f_{\text{cs}}$ ,  $f_{\text{ss}}$ ,  $y_g$  and  $\alpha = 10$  to calculate the model correlation function of Section 4. We split the halos in the interval  $M \in [10.9, 15]$  with bin width  $dM = 0.036$ .

In the top-left panel of Figure 4, the blue dots represent the measured galaxy two-point correlation function  $\xi_{gg}^{\text{mea}}$  of the DARK SAGE simulation.<sup>6</sup> Its comparison with the observational measurements from Martin et al. (2012) is shown in Figure 5. Martin et al. (2012) measures the H I-selected galaxy two-point correlation function from the  $\alpha.40$  sample of ALFALFA (Haynes et al. 2011). Our measurements are in agreement with Martin et al. (2012), indicating that  $\xi_{gg}$  from DARK SAGE serves as an appropriate proxy for that of an H I survey for our HOD-fitting method.

The HOD parameters are fitted by minimizing the  $\chi^2$  between  $\xi_{gg}^{\text{mea}}$  and  $\xi_{gg}^{\text{mod}}$ , given by

$$\chi^2 = (\xi_{gg}^{\text{mea}} - \xi_{gg}^{\text{mod}}) \mathbf{C}^{-1} (\xi_{gg}^{\text{mea}} - \xi_{gg}^{\text{mod}})^T, \quad (16)$$

where  $\mathbf{C}$  is the jackknife covariance matrix, expressed as (Escoffier et al. 2016)

$$\mathbf{C}_{ij} = \frac{N_s - N_d}{N_d N_{JK}} \sum_{k=1}^{N_{JK}} (\xi_{gg}^{\text{mea},ik} - \bar{\xi}_{gg}^{\text{mea},i})(\xi_{gg}^{\text{mea},jk} - \bar{\xi}_{gg}^{\text{mea},j}). \quad (17)$$

<sup>6</sup> We calculate this using the PYTHON package CorrFunc; <https://corrfunc.readthedocs.io/en/master/>.

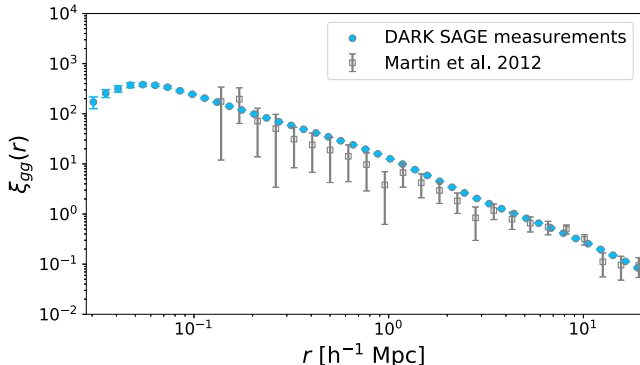


**Figure 5.** Comparison between the  $\xi_{gg}^{\text{mea}}$  of DARK SAGE (blue dots) and the observational measurements from Martin et al. (2012; gray squares).

Following the arguments in Escoffier et al. (2016), we divide the simulation box into  $N_s = 8$  identical sized cubes, then randomly delete  $N_d = 4$  cubes to obtain  $N_{JK} = 70$  jackknife samples.  $\xi_{gg}^{\text{mea},i}$  is the average of  $\xi_{gg}^{\text{mea}}$  of the  $N_{JK}$  jackknife samples in the  $i^{\text{th}}$  separation bin.

The Metropolis-Hastings Markov chain Monte Carlo (MCMC) algorithm is applied to estimate the HOD parameters. We use flat priors in the interval  $M_1 \in [11, 13]$ ,  $\beta \in [0.7, 1.5]$ , and  $M_{\text{cut}} \in [10, 11]$ .

The fit results are shown in Figure 4. The estimated HOD parameters are  $\beta = 0.9716^{+0.0032}_{-0.0035}$ ,  $M_1 = 12.2858^{+0.0058}_{-0.0050}$ , and  $M_{\text{cut}} = 11.0292^{+0.027}_{-0.030}$ . Plugging these best-fit values into Equation (15), we obtain the HOD of satellite galaxies predicted by the galaxy two-point correlation function, as shown in the bottom-left panel of Figure 4. The predicted HOD from fitting the galaxy clustering is in excellent agreement with the measured HOD, which validates our pipeline and the use of the measured central and satellite profiles in our fitting. In the bottom-left panel of Figure 4, there is a slight disagreement between the measured and predicted HODs below  $M = 11.25$ . This is due to the imperfect fit of the model correlation function in smaller separation bins ( $r < 0.05 h^{-1} \text{ Mpc}$ ), arising from the combination of measurement error in the correlation function and in our theoretical model, which relies on noisy measurements of  $f_{ss}$  and  $f_{cs}$ . The presence of noise in our theory prediction is not accounted for in the covariance matrix, and so it leads to this small disagreement. However, this is a small enough effect that we do not deem necessary to fix. If instead we were to use the analytic  $f_{ss}$  and  $f_{cs}$  of the NFW profile as the input of the model correlation function, the predicted HOD would have a significantly higher one-halo term, which would lead to a larger amplitude,  $M_1$ , and larger mass limit,  $M_{\text{cut}}$ , as well as smaller slope  $\beta$ . However, it more generally also leads to difficulty fitting both the one- and two-halo parts of the correlation function simultaneously.

## 6. Application as a Function of the HI Mass

In this section, we take our HOD-fitting methodology and apply it to different HI mass bins within the simulation.

### 6.1. Checking the Form of the HI-conditional HOD Model

Before fitting the HI-conditional HOD models using the galaxy two-point correlation function, we need to explore how well the functional forms of Equations (3a) and (3b) compare to the measured HOD in different mass bins. Therefore, we

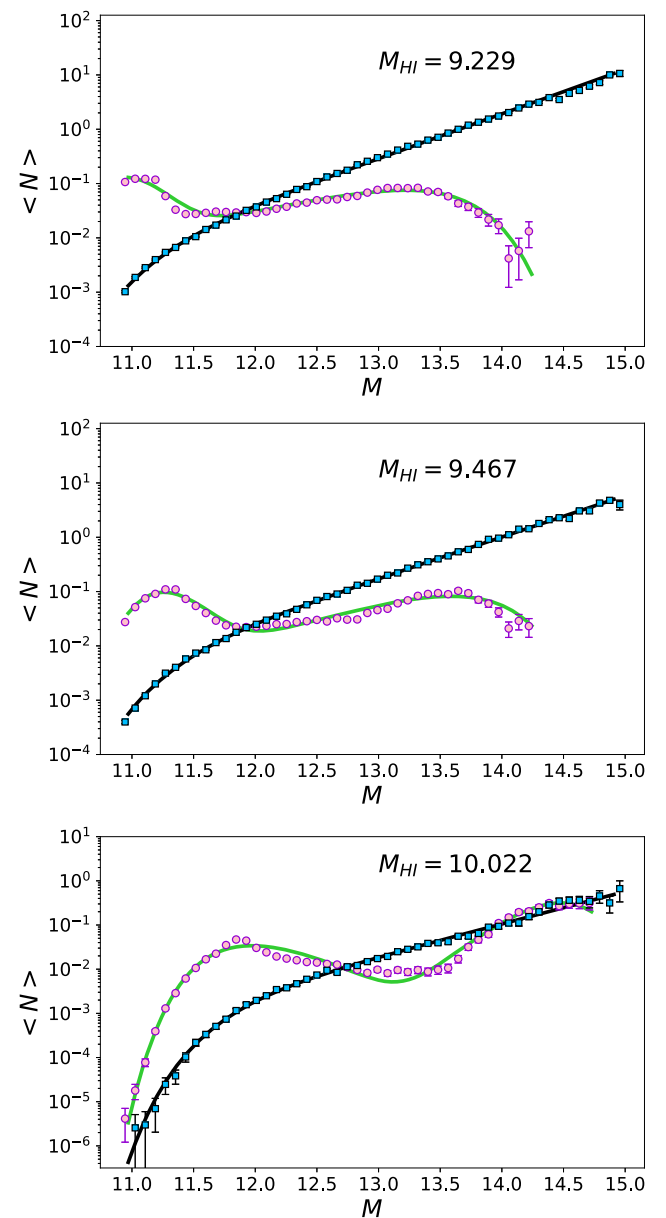


**Figure 6.** Fits of our model HOD, Equations (3a) and (3b), to the measured HOD. Three example  $M_{\text{HI}}$  bins are shown. The black and green curves are the best-fit satellite and central models, respectively, while the blue squares and purple circles show the measurements from these two classes of galaxy.

directly fit Equations (3a) and (3b) to the measured HOD. To measure the HOD, we divide the halo mass into 50 bins in the interval  $M \in [10.9, 15]$ . Then in each halo mass bin, we divide the HI mass in the interval  $M_{\text{HI}} \in [9.11, 10.3]$  with bin width  $dM_{\text{HI}} = 0.079$ . The fit results for three example mass bins are shown in Figure 6. Our model curves can fit the central and satellite HODs remarkably well over a range of HI and halo mass bins, which indicates that our HOD model is flexible enough to fit the data.

### 6.2. Reducing the Parameters of the HI-conditional HOD Model of the Central Galaxies

When fitting the HOD model to the various mass bins, we introduce a large number of free parameters (9 per HI mass bin, so a total of 135 over the entire simulation). This could present

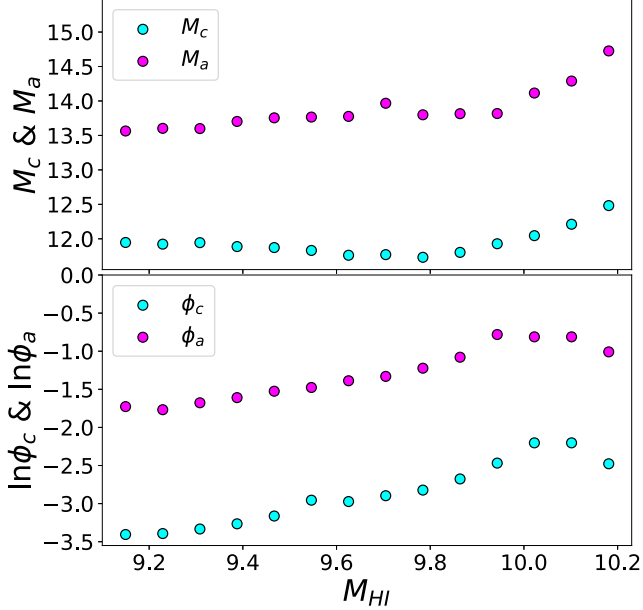


**Figure 7.** Best-fit values of HOD parameters  $M_c$ ,  $M_a$ ,  $\phi_c$ , and  $\phi_a$  as functions of the H I mass.

a problem when fitting the clustering, due to difficulties optimizing in such a high-dimension parameter space, which introduces a high chance of overfitting. So, initially, we investigate whether there are any trends in the best-fit HOD parameters between H I mass bins that can enable us to simplify the model.

First, we find particularly interesting correlations between two pairs of parameters shown in Figure 7. For one, we find that  $M_a$  shows an almost constant shift compared to  $M_c$ . We also then see that  $\ln \phi_a$  shows an approximately constant shift compared to  $\ln \phi_c$  too. These pairs of parameters are the locations and relative amplitudes of the two “knees” of the double Schechter function used to parameterize the central galaxy HOD.

Given the relation between these pairs, we can reduce the number of parameters of Equation (3a) by setting

$$M_a = M_c + 2, \quad \phi_a = 5\phi_c. \quad (18)$$

We are then left with only 7 free parameters per H I mass bin (or 105 for the full simulation). For these remaining parameters, we plot the fit results against the mean H I mass in each bin in Figure 8.

Looking at these, we see that they nearly all present as (close to) linear or quadratic functions of the H I mass. We hence implement our H I-mass-conditional HOD by enforcing relationships between parameters  $\mathbf{P} = \{M_c, \beta_1, \ln \beta_2, \ln \phi_c, \beta_s, \phi_s\}$  and  $M_{\text{HI}}$  using linear functions,

$$\mathbf{P}_i = k_i M_{\text{HI}} + b_i. \quad (19)$$

While  $M_s$  is a quadratic function of the H I mass,

$$M_s = c_0 + c_1 M_{\text{HI}} + c_2 M_{\text{HI}}^2, \quad (20)$$

Fitting our HOD parameters as a function of the H I mass, we recover the black lines in Figure 8. The best-fit values of  $(k_i, b_i)$  are given in the first two columns of Table 1 while  $c_0 = 42.748$ ,  $c_1 = -7.352$ ,  $c_2 = 0.426$ .

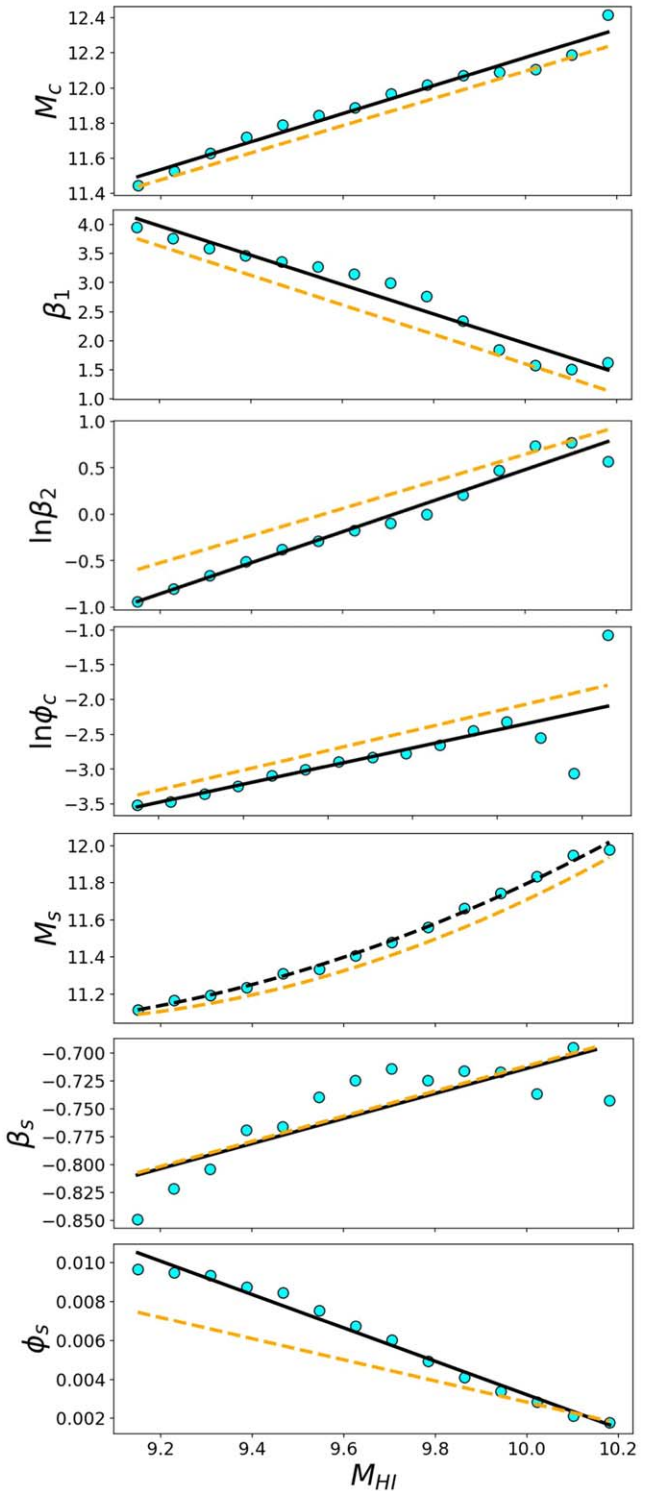


**Figure 8.** Parameters of Equations (3a) and (3b) as functions of the H I mass. The blue filled circles are the parameters fitted by comparing the model HOD to the measured HOD in each H I mass bin. The black lines and curve are the best fits to the blue filled circles, resulting in our 15 “hyperparameters”. The orange dashed lines and curve are the best-fit results obtained by comparing model  $\xi_{\text{ee}}$  to the measured  $\xi_{\text{ee}}$ . Differences between this figure and Figure 7 for overlapping parameters arise due to the fact that we have forced the remaining two of the parameters of the full HOD model (not plotted here) to follow Equation (18), which was not the case for Figure 7.

With the above procedure, we have reduced the full set of 135 HOD parameters in our model down to only 15 “hyperparameters”. Our parameterization directly maps the

**Table 1**

Best-fit values of  $k$  and  $b$  from Equation (19) for each relevant HOD parameter both from fitting the measured HODs in each H<sub>I</sub> mass bin directly (Section 6.2) and from fitting the galaxy correlation functions (Section 6.3)

| $P$           | Fit from the measured HOD |         | Fit from $\xi_{gg}$ |         |
|---------------|---------------------------|---------|---------------------|---------|
|               | $k_i$                     | $b_i$   | $k_i$               | $b_i$   |
| $M_c$         | 0.799                     | 4.183   | 0.774               | 4.353   |
| $\beta_1$     | -2.528                    | 27.234  | -2.538              | 26.981  |
| $\ln \beta_2$ | 1.678                     | -16.295 | 1.459               | -13.948 |
| $\ln \phi_c$  | 1.302                     | -15.453 | 1.419               | -16.353 |
| $\beta_s$     | 0.112                     | -1.838  | 0.112               | -1.839  |
| $\phi_s$      | -0.00858                  | 0.0890  | -0.00544            | 0.0572  |

halo mass to the number of galaxies *of a given H<sub>I</sub> mass* and so can be used to populate halos not just with a number of galaxies (as in a standard HOD), but assign H<sub>I</sub> masses to those galaxies too. For example, by plugging  $M_{HI} = 9.229$  into Equations (19) and (20) one can obtain HOD parameters  $M_c$ ,  $\beta_1$ ,  $\beta_2$ ,  $\phi_c$  and  $M_s$ ,  $\beta_s$ ,  $\phi_s$ . These can then be plugged into Equations (18), (3a), and (3b) to obtain the HOD of central and satellite galaxies, with the results shown in the top panel of Figure 9. Another two example H<sub>I</sub> mass bins are also shown in Figure 9. Overall, after exploring all H<sub>I</sub> mass bins, we find that the HOD calculated from the H<sub>I</sub> mass using this procedure still matches the measured HOD exceptionally well despite the large reduction in the number of free parameters we need.

We caution that the exact values of the  $(k_i, b_i)$  and  $c_0, c_1, c_2$ , and the constant relations seen in Equation (18) are specific to the DARK SAGE simulation. However, we believe that enough flexibility remains for the same model to fit real data, given that the simulation reproduces the  $z=0$  H<sub>I</sub> mass function, stellar mass function, and H<sub>I</sub> mass-to-stellar mass ratio of the real universe (Stevens et al. 2018). It would hence be interesting to explore if this is the case, and whether changes to the exact functional forms described above are needed. However, we leave this for the next work in the series, and for the remainder of this paper demonstrate that the conditional HOD described above can also be constrained purely from measurements of the galaxy clustering, without requiring prior knowledge of the halo masses themselves.

### 6.3. Fitting the H<sub>I</sub>-conditional HOD Using the Galaxy Two-point Correlation Function

We test our model further by fitting the measured two-point correlation functions for the galaxies in each H<sub>I</sub> mass bin from Section 6.1, concatenating them together to obtain a single data vector. For a given set of HOD parameters  $k_i, b_i, c_0, c_1, c_2$ , we calculate the HOD models for each H<sub>I</sub> mass bin using Equations (19), (20), (18), (3a), and (3b). We then calculate the model correlation function in each H<sub>I</sub> mass bin using the methodology of Section 4 and measured radial profiles for the simulation shown in Section 5.1, before again concatenating them together to obtain a single model vector. Finally, we minimize the difference between the data and model to find the best-fitting  $k_i, b_i, c_0, c_1, c_2$ .

In this case, we are using the least squares difference rather than  $\chi^2$  minimization to fit the model correlation functions to the measurements as it is not possible to estimate the full

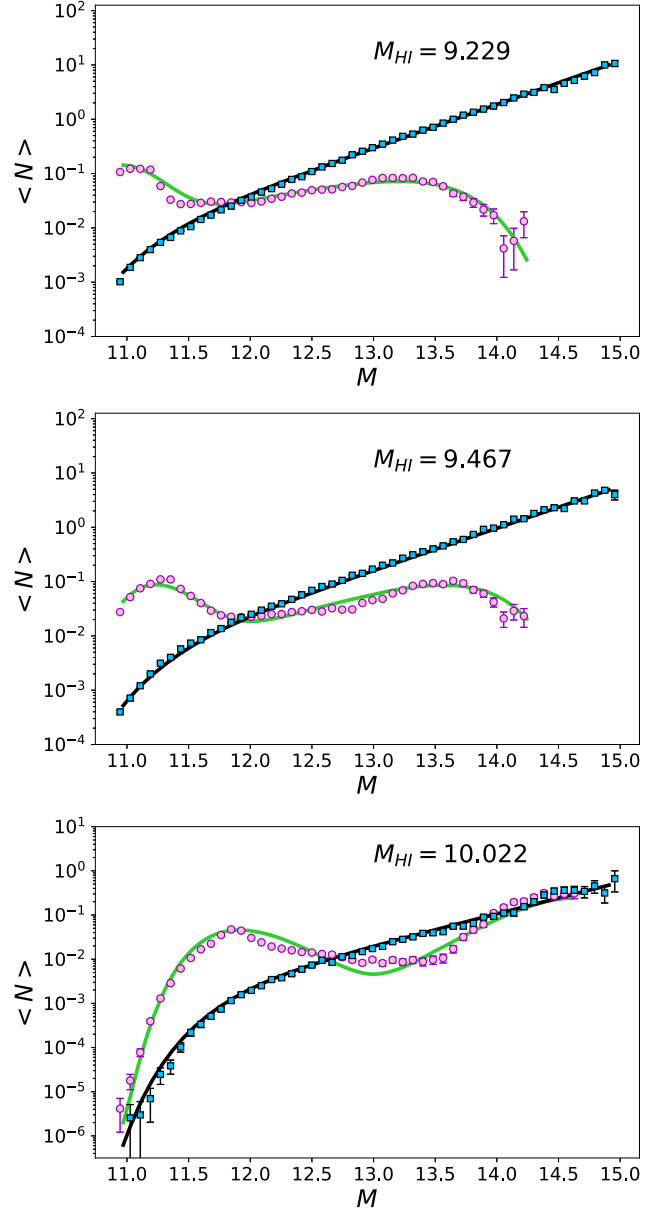


**Figure 9.** Comparison of the model HOD (green and black curves for central and satellite galaxies, respectively) predicted by our 15 best-fit “hyperparameters” and the measured HOD (pink circles and blue squares for centrals and satellites, respectively) for three example  $M_{HI}$  bins. This plot looks functionally very similar to Figure 6, which emphasizes the fact that we are able to recover well the measured HODs for various H<sub>I</sub> mass bins using our “hyperparameters”, rather than fitting each bin individually.

covariance matrix of the correlation function using a single DARK SAGE simulation and jackknife. There are over 500 correlated measurement bins, far larger than the number of jackknife samples we could generate, leading to a noisy and ill-conditioned estimate of the covariance matrix. In future work, we will develop a more robust method for the fitting that iterates between populating an ensemble of simulations with an HOD, using this ensemble to estimate the covariance matrix, and then fitting the data to generate the next HOD with which to populate the ensemble (i.e., as done in Howlett et al. 2015a, 2022; Qin et al. 2019a, 2021). Nonetheless, the methodology used here is sufficient for the purposes of this proof-of-concept study.

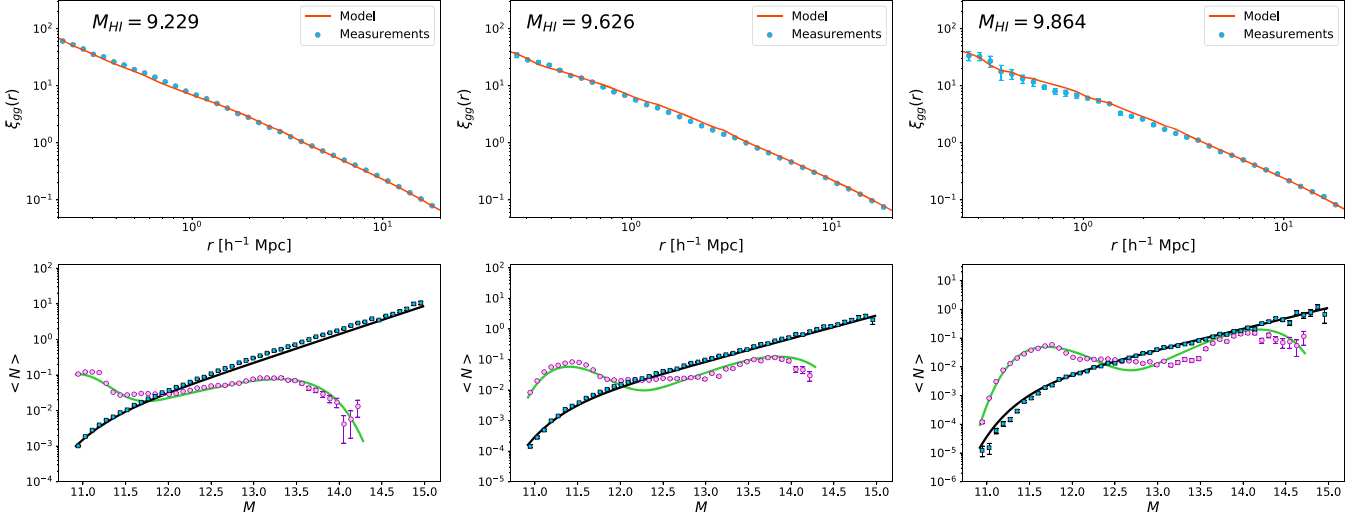


**Figure 10.** Demonstration of fitting the HOD of H I galaxies using the galaxy two-point correlation function. Three example  $M_{\text{HI}}$  bins are shown. The panels in the top row show the measured and modeled correlation functions (blue circles and red curves, respectively). The bottom panels show the measured HOD for centrals and satellites (pink circles and blue squares, respectively) against that predicted (green/black curves for centrals/satellites) by our best-fitting set of “hyperparameters” obtained from fitting the correlation functions.

The above fitting method can be applied to real galaxy surveys too. For example, in the WALLABY data, the H I masses of hundreds of thousands of galaxies will be measured in the mass range we have studied here (Koribalski et al. 2020). Therefore, the two-point correlation functions of the galaxies in each H I mass bin can be measured and then fitted to the model correlation functions to estimate the HOD parameters in the same fashion as the simulation data. This is in fact crucial to understanding the relationship between H I galaxies and their host halos, as if we were to measure and fit only a single correlation across all WALLABY galaxies, we would be only able to constrain the total H I-to-halo mass ratio (i.e., as in Obuljen et al. 2019—see Appendix C), rather than how that total H I mass is distributed across individual central and satellite galaxies.

In Figure 10 we show the results from simultaneously fitting all 15 correlation functions with our conditional HOD model containing 15 free parameters. Although we are unable to report a chi-squared for the fit, we find models for the correlation functions that agree well visually across all the scales and H I mass bins we consider. More remarkable is the agreement seen in the lower panels of this figure between the measured HOD of each H I mass bin and that *predicted* from fitting the correlation functions. We see model HODs that align well with the measurements, despite us having the equivalent of only a single parameter per bin. We reiterate that we have not allowed the HOD parameters in each bin to vary independently but rather are forcing the parameters describing the shapes of the various Schechter functions to themselves depend only linearly or quadratically on the value of  $M_{\text{HI}}$  for a given bin. We hence are able to fit the many correlation functions without any knowledge of the halo masses themselves, only the mean H I mass.

The recovered linear and quadratic functions of H I mass are shown as the dashed orange lines and curve in Figure 8. The best estimated values of  $k_i$ ,  $b_i$  are listed in the last two columns of Table 1, while  $c_0 = 51.321$ ,  $c_1 = -9.084$ ,  $c_2 = 0.512$ . Here, we do see some differences between the parameters obtained from directly fitting the measured HOD, and those *inferred*

from fitting the correlation functions. These arise primarily due to (1) degeneracies across the full parameter space, which mean that multiple values of our fitting parameters can return similar correlation functions; (2) noise in the measured  $\xi_{\text{gg}}$ , at large separations (due to the finite volume of the simulation), or at small separation/bins with larger H I mass (due to shot noise); and (3) noise in the *model*  $\xi_{\text{gg}}$ , especially in larger H I mass bins with fewer galaxies, due to the use of measured radial distributions for the simulated halos. Nevertheless, our method is still able to reproduce the clustering of the H I galaxies well.

One very interesting by-product of fitting the H I-conditional HOD using the galaxy clustering is that we can take an HOD model and integrate over the halo mass to recover a prediction for the H I mass function of galaxies. As a final check of our method we do this for our best fit above and compare to the H I mass function measured from the DARK SAGE simulation. This is shown in Figure 11. Again, despite not including the H I mass function in our fit, we find good agreement between the measurements and predictions, both for all galaxies and when split into separate central and satellite populations. We note that this agreement could be made even better by including the observed H I mass function alongside the correlation functions in our joint data vector, which we anticipate would break some of the degeneracies between our “hyperparameters” and result in greater agreement between the measurements and predictions in Figure 8. However, we find it more revealing to leave this as a cross validation for now and defer including it in the fit to future work.

## 7. Conclusion

In this paper, we have presented a new HOD model for H I galaxies, using single and double Schechter functions that predict the number of central and satellite galaxies (Equations (3a) and (3b)) in a halo, and functions of the neutral hydrogen mass ( $M_{\text{HI}}$ ) that predict the parameters of these Schechter functions (encapsulated by Equations (18), (19), and (20)). In much the same way as the conditional luminosity or stellar mass functions (Cooray 2006; Guo et al. 2018), this enables us to predict the number of galaxies of a

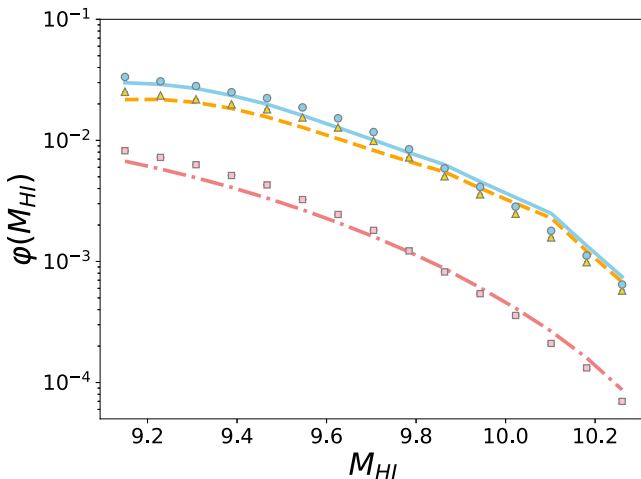


**Figure 11.** Measured H I mass function of DARK SAGE (points) compared to the mass function predicted (lines) by integrating over our best-fit conditional HOD (with parameters given in the last two columns of Table 1). Blue points and curves are the total mass function, which we further split into centrals (yellow) and satellites (pink). The error bars are tiny.

given H I mass in halos of a given halo mass, and so produce mock catalogs that contain H I masses in addition to positions and velocities. This will be crucial for constraining the cosmology from upcoming radio surveys such as WALLABY (Koribalski et al. 2020) or with SKA (Square Kilometre Array Cosmology Science Working Group et al. 2020).

The functional form used for the HOD model contains a total of 15 free parameters and is determined from comparison with the DARK SAGE simulation. We have demonstrated that these parameters can be fit well to the galaxy correlation function measured in H I mass bins and that applying this to the simulation results in good agreements between the measured and predicted conditional HOD and H I mass function. This is encouraging, as it means one could consider making such measurements with real data, fitting these to obtain the best-fit HOD parameters, and then using these to populate simulations in a way that reproduces the clustering and H I mass function of the data.

One caveat to our work is that we found the model to be very sensitive to the assumed radial distribution of satellite galaxies in their host halos, as any HOD model would be. We measured the radial profile of the H I galaxies in the DARK SAGE simulation and found that they do not follow the NFW profile. Hence, accurately calculating the model correlation function requires us to use the measured radial profiles rather than analytic.

There are many extensions to this first work that can be pursued, including further investigation of the impact of the halo radial profiles on the conditional HOD, the inclusion of H I mass function as data to constrain the HOD parameters, and improvements to the overall robustness of the fitting method we use here (e.g., properly accounting for the covariance between correlation function measurements). We also restricted our analysis to real-space positions of galaxies measured from the simulation. In future work, we aim to improve on these and develop a complete mock sampling algorithm for H I surveys that can be used to generate mocks, for example, for the redshift and Tully–Fisher catalogs of WALLABY (Koribalski et al. 2020). For example, we anticipate that a simple extension would be to use a light-cone simulation with galaxy redshifts to

measure and model the redshift-space clustering by also drawing radial velocities (from the NFW profile, or other suitable distribution) alongside positions when populating the halos with galaxies (as in Howlett et al. 2015b, 2022; Qin et al. 2021).

F.Q. and D.P. are supported by the project 우주거대구조를 이용한 암흑우주 연구 (“Understanding Dark Universe Using Large Scale Structure of the Universe”), funded by the Ministry of Science. C.H. is supported by the Australian Government through the Australian Research Councils Laureate Fellowship funding scheme (project FL180100168). ARHS is funded through the Jim Buckee Fellowship at ICRAR-UWA.

*Software:* CAMB (Lewis et al. 2000), CHAINCONSUMER (Hinton 2016), CORRFUNC (Sinha & Garrison 2020), DARK SAGE (Stevens et al. 2017), EMCEE (Foreman-Mackey et al. 2013), MATPLOTLIB (Hunter 2007), NBODYKIT (Hand et al. 2018), SCIPY (Virtanen et al. 2020).

## Appendix A The Halo Biasing Parameter

The halo biasing parameter  $b_h(M)$  is defined as (Tinker et al. 2005)

$$b_h^2(M) \equiv \frac{\xi_h(r, M)}{\xi_m(r)}, \quad (A1)$$

where  $\xi_h(r, M)$  is the two-point correlation function of the halos of mass  $M$ , while  $\xi_m(r)$  is the nonlinear matter correlation function. We use the CAMB package to generate the nonlinear matter power spectrum and then convert it into the nonlinear matter correlation function.<sup>7</sup>

Following the arguments in Appendix A of Tinker et al. (2005), to measure the halo biasing parameter of DARK SAGE simulation, we first divide the parent halos into 30 mass bins and then measure  $\xi_h(r, M)$  of the halos in each mass bin. Finally, we calculate  $b_h$  in each halo mass bin by averaging  $\sqrt{\xi_h/\xi_m}$  for pair separations  $4 \leq r h/\text{Mpc} \leq 15$ . In this interval, the ratio between the halo and matter correlation functions is approximately constant, and the measured correlation functions are smooth. In Figure 12, the blue dots represent the measured halo biasing parameters as a function of  $\nu = \delta_c/\sigma(m)$ , where the critical density contrast for collapse is  $\delta_c = 1.686$ .

The model halo biasing parameter can be written as (Sheth et al. 2001; Yang et al. 2003; Tinker et al. 2005; Zheng & Weinberg 2007)

$$b_h(\nu) = 1 + \frac{1}{\sqrt{a} \delta_c} \times \left[ \sqrt{a} (a\nu^2) + \sqrt{a} b (a\nu^2)^{1-q} - \frac{(a\nu^2)^q}{(a\nu^2)^q + b(1-q)(1-q/2)} \right]. \quad (A2)$$

Fitting the model to the measurements, we find  $a = 0.79168$ ,  $b = 0.21136$ , and  $q = 0.66108$  for DARK SAGE, which differs slightly from the values found in (Tinker et al. 2005). The measurements, our best-fit model, and the Tinker et al. (2005) model are shown in Figure 12.

<sup>7</sup> We use the function `cosmology.pk_to_xi` of the `PYTHON` package `Nbodykit`. [https://nbodykit.readthedocs.io/en/latest/api/\\_autosummary/nbodykit.cosmology.correlation.html](https://nbodykit.readthedocs.io/en/latest/api/_autosummary/nbodykit.cosmology.correlation.html).

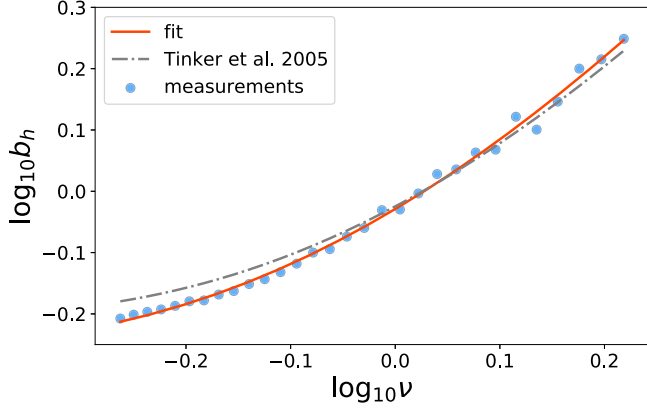


**Figure 12.** Halo biasing parameter as a function of  $\nu = \delta_c / \sigma(m)$ . The blue dots are the measured halo biasing parameters of the DARK SAGE simulation, the red curve is the model fit to the measurements, and the gray curve is the fit from Tinker et al. (2005).

## Appendix B NFW Halo Density Profile

A commonly used halo density profile for the matter is the Navarro–Frenk–White (NFW) profile (Navarro et al. 1996, 1997), and the radial distribution of the mass density is given by Navarro et al. (1996, 1997), Yang et al. (2003), and Zheng & Weinberg (2007)

$$\rho_m(R) = \frac{\rho_s}{(R/R_s)(1+R/R_s)^2}, \quad (\text{B1})$$

where

$$\rho_s = \frac{\rho_0 \Delta}{3} \frac{c^3}{\ln(1+c) - c/(1+c)}, \quad (\text{B2})$$

and the halo concentration is defined as

$$c \equiv \frac{R_{\text{vir}}}{R_s}. \quad (\text{B3})$$

$R_s$  is the break radius between the outer and inner density profiles of the halo. We use the fitting formulae of Prada et al. (2012; Section 5 therein) to calculate  $c$  for the halos as a function of the halo mass for the DARK SAGE cosmology.

The radial profile Equation (B1) gives the radial distribution of matter within halos, but we also need the radial distribution of galaxies, and these two may not be the same. In the one-halo term of the two-point correlation function given in Equation (5), the radial distribution is expressed as the halo center-to-satellite density function  $f_{\text{cs}}(x)$  and the satellite-to-satellite radial density function  $f_{\text{ss}}(x)$ . If we assume an NFW profile and set  $\alpha = 2$  (Berlind & Weinberg 2002; Tinker et al. 2005; Zheng & Weinberg 2007), then  $\rho_m(r)$  in Equation (8) is given by Equation (B1). The expression for  $f_{\text{ss}}(x)$  is given in Appendix A of Zheng & Weinberg (2007) but is lengthy and so not repeated here.

Plugging Equations (B1) and (B2) into Equation (14), one can obtain the Fourier transformation of the NFW density,

analytically expressed as (Cooray & Sheth 2002)

$$y_g(k) = \frac{1}{\ln(1+c) - c/(1+c)} \times \left\{ -\frac{\sin(ckR_s)}{(1+c)kR_s} \right. \\ \left. + \sin(kR_s)[SI([1+c]kR_s) - SI(kR_s)] \right. \\ \left. + \cos(kR_s)[CI([1+c]kR_s) - CI(kR_s)] \right\}, \quad (\text{B4})$$

and where

$$SI(x) \equiv \int_0^x \frac{\sin t}{t} dt, \quad (\text{B5a})$$

$$CI(x) \equiv -\int_x^\infty \frac{\cos t}{t} dt, \quad (\text{B5b})$$

are the so-called trigonometric integrals. This expression is used to calculate  $y_g(k)$  of the NFW profile in Figure 3.

## Appendix C The H I-halo Mass Relation

A predicted quantity of our H I HOD that we did not assess in the main text is the H I-halo mass relation (HIHMR). The HIHMR describes the *total* H I content of a halo, that is, the summed H I content of all galaxies in a halo. In principle, this should also include H I in the circumgalactic/intracluster medium (see, e.g., the results of Stevens & Diemer 2019b; van de Voort et al. 2019; Garratt-Smithson & Power 2021), but here we assume this to be negligible. In Figure 13, we compare the *mean* HIHMR from DARK SAGE and our HOD fitted to it with that derived from observations.

The yellow filled circles show the HIHMR measured from the direct output of DARK SAGE. The blue curve is the HIHMR predicted by the best-fit conditional HOD (with parameters given in the last two columns of Table 1). Reassuringly, we find good agreement between the measurements and prediction.

The gray squares and the black points display the HIHMR data from Obuljen et al. (2019) and Guo et al. (2020), respectively. Obuljen et al. (2019) use the  $\alpha_{40}$  sample of ALFALFA, while Guo et al. (2020) use the ALFALFA catalog from Haynes et al. (2018). They estimate the H I masses in dark matter halos from galaxy groups. Guo et al. (2020) used  $2R_{\text{vir}}$  with  $\Delta = 200$  as the aperture for groups, while Obuljen et al. (2019) used  $2R_{\text{vir}}$  with  $\Delta = 180$  as their aperture (see Equation (7)).

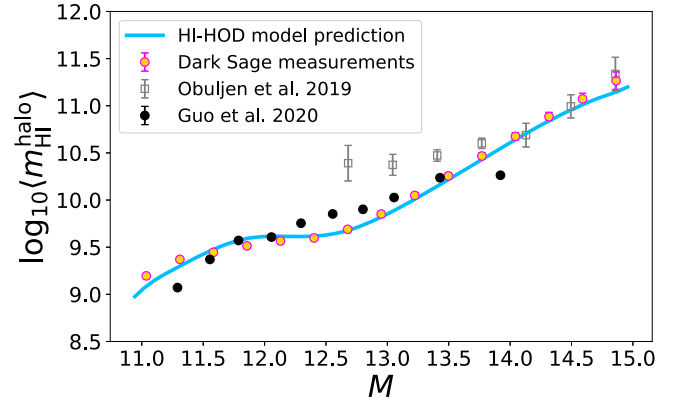


**Figure 13.** Mean H I content of halos (inside  $2R_{\text{vir}}$ ) as a function of the virial mass. Compared are the direct output of DARK SAGE, the prediction from our H I-conditional HOD (fitted to DARK SAGE data but not this relation in particular), and two observational data sets based on the ALFALFA survey (Obuljen et al. 2019; Guo et al. 2020).

At higher halo masses, we find good agreement between our measurements and the observed values from Obuljen et al. (2019). Our measurements are generally in reasonable agreement with the observed values from Guo et al. (2020). At lower halo masses, our measurements are slightly higher than the values from Guo et al. (2020). Due to the observation limit of faint galaxies, the less massive galaxies of smaller groups might be missed in Guo et al. (2020), resulting in the underestimated HIHMR in smaller halo mass bins (see Section 4.2 of their paper for further discussion). For a fair comparison to Obuljen et al. (2019) and Guo et al. (2020), we removed the satellites that are beyond  $2R_{\text{vir}}$  to measure the HIHMR. For a more in-depth comparison method to the Guo et al. (2020) data for a semi-analytic model, see Chauhan et al. (2021).

## ORCID iDs

Fei Qin <https://orcid.org/0000-0001-7950-7864>  
 Cullan Howlett <https://orcid.org/0000-0002-1081-9410>  
 Adam R. H. Stevens <https://orcid.org/0000-0003-1908-2168>  
 David Parkinson <https://orcid.org/0000-0002-7464-2351>

## References

Avila, S., Gonzalez-Perez, V., Mohammad, F. G., et al. 2020, *MNRAS*, **499**, 5486  
 Avila, S., Vos-Ginés, B., Cunningham, S., et al. 2022, *MNRAS*, **510**, 292  
 Baldry, I. K., Glazebrook, K., & Driver, S. P. 2008, *MNRAS*, **388**, 945  
 Berlind, A. A., & Weinberg, D. H. 2002, *ApJ*, **575**, 587  
 Beutler, F., Blake, C., Colless, M., et al. 2012, *MNRAS*, **423**, 3430  
 Blake, C., Carter, P., & Koda, J. 2018, *MNRAS*, **479**, 5168  
 Blot, L., Crocce, M., Sefusatti, E., et al. 2019, *MNRAS*, **485**, 2806  
 Brown, T., Catinella, B., Cortese, L., et al. 2015, *MNRAS*, **452**, 2479  
 Calette, A. R., Rodríguez-Puebla, A., Avila-Reese, V., & Lagos, C. d. P. 2021, *MNRAS*, **506**, 1507  
 Carrick, J., Turnbull, S. J., Lavaux, G., & Hudson, M. J. 2015, *MNRAS*, **450**, 317  
 Castorina, E., & Villaescusa-Navarro, F. 2017, *MNRAS*, **471**, 1788  
 Chauhan, G., Lagos, C. d. P., Stevens, A. R. H., et al. 2020, *MNRAS*, **498**, 44  
 Chauhan, G., Lagos, C. d. P., Stevens, A. R. H., et al. 2021, *MNRAS*, **506**, 4893  
 Cole, S., Percival, W. J., Peacock, J. A., et al. 2005, *MNRAS*, **362**, 505  
 Cooray, A. 2006, *MNRAS*, **365**, 842  
 Cooray, A., & Sheth, R. 2002, *PhR*, **372**, 1  
 Croton, D. J., Stevens, A. R. H., Tonini, C., et al. 2016, *ApJS*, **222**, 22  
 Dupuy, A., Courtois, H. M., Graziani, R., & Kubik, B. 2019, *MNRAS*, **486**, 440  
 Escoffier, S., Cousinou, M. C., Tilquin, A., et al. 2016, arXiv:1606.00233  
 Feldman, H. A., Kaiser, N., & Peacock, J. A. 1994, *ApJ*, **426**, 23  
 Foreman-Mackey, D., Hogg, D. W., Lang, D., & Goodman, J. 2013, *PASP*, **125**, 306  
 Fu, J., Kauffmann, G., Huang, M. -L., et al. 2013, *MNRAS*, **434**, 1531  
 Garratt-Smithson, L., Power, C., Lagos, C. d. P., et al. 2021, *MNRAS*, **501**, 4396  
 Giovanelli, R., Haynes, M. P., Kent, B. R., et al. 2005, *AJ*, **130**, 2598  
 Gonzalez-Perez, V., Comparat, J., Norberg, P., et al. 2018, *MNRAS*, **474**, 4024  
 Gorski, K. M., Davis, M., Strauss, M. A., White, S. D. M., & Yahil, A. 1989, *ApJ*, **344**, 1  
 Guo, H., Jones, M. G., Haynes, M. P., & Fu, J. 2020, *ApJ*, **894**, 92  
 Guo, H., Yang, X., & Lu, Y. 2018, *ApJ*, **858**, 30  
 Guo, H., Zehavi, I., Zheng, Z., et al. 2013, *ApJ*, **767**, 122  
 Guo, H., Zheng, Z., Zehavi, I., et al. 2014, *MNRAS*, **441**, 2398  
 Guo, H., Zheng, Z., Zehavi, I., et al. 2015a, *MNRAS*, **446**, 578  
 Guo, H., Zheng, Z., Zehavi, I., et al. 2015b, *MNRAS*, **453**, 4368  
 Hadzhiyska, B., Tacchella, S., Bose, S., & Eisenstein, D. J. 2021, *MNRAS*, **502**, 3599  
 Hand, N., Feng, Y., Beutler, F., et al. 2018, *AJ*, **156**, 160  
 Hatton, S., & Cole, S. 1998, *MNRAS*, **296**, 10  
 Haynes, M. P., Giovanelli, R., Kent, B. R., et al. 2018, *ApJ*, **861**, 49  
 Haynes, M. P., Giovanelli, R., Martin, A. M., et al. 2011, *AJ*, **142**, 170  
 Hinton, S. R. 2016, *JOSS*, **1**, 00045  
 Hong, T., Staveley-Smith, L., Masters, K. L., et al. 2019, *MNRAS*, **487**, 2061  
 Howlett, C. 2019, *MNRAS*, **487**, 5209  
 Howlett, C., Lewis, A., Hall, A., & Challinor, A. 2012, *JCAP*, **2012**, 027  
 Howlett, C., Manera, M., & Percival, W. J. 2015a, *A&C*, **12**, 109  
 Howlett, C., Ross, A. J., Samushia, L., Percival, W. J., & Manera, M. 2015b, *MNRAS*, **449**, 848  
 Howlett, C., Said, K., Lucey, J. R., et al. 2022, *MNRAS*, **515**, 953  
 Hunter, J. D. 2007, *CSE*, **9**, 90  
 Jenkins, A., Frenk, C. S., White, S. D. M., et al. 2001, *MNRAS*, **321**, 372  
 Jing, Y. P., Mo, H. J., & Börner, G. 1998, *ApJ*, **494**, 1  
 Johnson, A., Blake, C., Koda, J., et al. 2014, *MNRAS*, **444**, 3926  
 Jones, M. G., Haynes, M. P., Giovanelli, R., & Moorman, C. 2018, *MNRAS*, **477**, 2  
 Knebe, A., Stoppacher, D., Prada, F., et al. 2018, *MNRAS*, **474**, 5206  
 Koda, J., Blake, C., Beutler, F., Kazin, E., & Marin, F. 2016, *MNRAS*, **459**, 2118  
 Koribalski, B. S., Staveley-Smith, L., Westmeier, T., et al. 2020, *Ap&SS*, **365**, 118  
 Kourkchi, E., Tully, R. B., Eftekharzadeh, S., et al. 2020, *ApJ*, **902**, 145  
 Lagos, C. d. P., Tobar, R. J., Robotham, A. S. G., et al. 2018a, *MNRAS*, **481**, 3573  
 Lagos, C. d. P., Tobar, R. J., Robotham, A. S. G., et al. 2018b, *Shark: Flexible semi-analytic galaxy formation model, Astrophysics Source Code Library*, [ascl:1811.005](https://ascl.net/1811.005)  
 Lewis, A., Challinor, A., & Lasenby, A. 2000, *ApJ*, **538**, 473  
 Maksimova, N. A., Garrison, L. H., Eisenstein, D. J., et al. 2021, *MNRAS*, **508**, 4017  
 Manera, M., Samushia, L., Tojeiro, R., et al. 2015, *MNRAS*, **447**, 437  
 Martin, A. M., Giovanelli, R., Haynes, M. P., & Guzzo, L. 2012, *ApJ*, **750**, 38  
 Martin, A. M., Papastergis, E., Giovanelli, R., et al. 2010, *ApJ*, **723**, 1359  
 Masters, K. L., Springob, C. M., & Huchra, J. P. 2008, *AJ*, **135**, 1738  
 McKee, C. F., & Krumholz, M. R. 2010, *ApJ*, **709**, 308  
 Navarro, J. F., Frenk, C. S., & White, S. D. M. 1996, *ApJ*, **462**, 563  
 Navarro, J. F., Frenk, C. S., & White, S. D. M. 1997, *ApJ*, **490**, 493  
 Obuljen, A., Alonso, D., Villaescusa-Navarro, F., Yoon, I., & Jones, M. 2019, *MNRAS*, **486**, 5124  
 Onions, J., Knebe, A., Pearce, F. R., et al. 2012, *MNRAS*, **423**, 1200  
 Padmanabhan, H., Refregier, A., & Amara, A. 2017, *MNRAS*, **469**, 2323  
 Paranjape, A., Choudhury, T. R., & Sheth, R. K. 2021b, *MNRAS*, **503**, 4147  
 Paranjape, A., Srianand, R., Choudhury, T. R., & Sheth, R. K. 2021a, [arXiv:2105.04570](https://arxiv.org/abs/2105.04570)  
 Paul, N., Choudhury, T. R., & Paranjape, A. 2018, *MNRAS*, **479**, 1627  
 Peacock, J. A., & Smith, R. E. 2000, *MNRAS*, **318**, 1144  
 Poulton, R. J. J., Power, C., Robotham, A. S. G., & Elahi, P. J. 2020, *MNRAS*, **491**, 3820  
 Prada, F., Klypin, A. A., Cuesta, A. J., Betancort-Rijo, J. E., & Primack, J. 2012, *MNRAS*, **423**, 3018  
 Qin, F., Howlett, C., & Staveley-Smith, L. 2019a, *MNRAS*, **487**, 5235  
 Qin, F., Howlett, C., Staveley-Smith, L., & Hong, T. 2019b, *MNRAS*, **482**, 1920  
 Qin, F., Parkinson, D., Howlett, C., & Said, K. 2021, *ApJ*, **922**, 59  
 Sheth, R. K., Mo, H. J., & Tormen, G. 2001, *MNRAS*, **323**, 1  
 Shi, F., Yang, X., Wang, H., et al. 2018, *ApJ*, **861**, 137  
 Sinha, M., & Garrison, L. H. 2020, *MNRAS*, **491**, 3022  
 Spergel, D. N., Verde, L., Peiris, H. V., et al. 2003, *ApJS*, **148**, 175  
 Springel, V., White, S. D. M., Jenkins, A., et al. 2005, *Natur*, **435**, 629  
 Stevens, A. R. H., & Brown, T. 2017, *MNRAS*, **471**, 447  
 Square Kilometre Array Cosmology Science Working Group, Bacon, D. J., Battye, R. A., et al. 2020, *PASA*, **37**, e007  
 Stevens, A. R. H., Croton, D. J., & Mutch, S. J. 2016, *MNRAS*, **461**, 859  
 Stevens, A. R. H., Croton, D. J., Mutch, S. J., & Sinha, M. 2017, *Dark Sage: Semi-analytic model of galaxy evolution, Astrophysics Source Code Library*, [ascl:1706.004](https://ascl.net/1706.004)  
 Stevens, A. R. H., Diemer, B., Lagos, C. d. P., et al. 2019a, *MNRAS*, **490**, 96  
 Stevens, A. R. H., Diemer, B., Lagos, C. d. P., et al. 2019b, *MNRAS*, **483**, 5334  
 Stevens, A. R. H., Lagos, C. d. P., Obreschkow, D., & Sinha, M. 2018, *MNRAS*, **481**, 5543  
 Strauss, M. A., & Willick, J. A. 1995, *PhR*, **261**, 271  
 Tinker, J. L., Weinberg, D. H., Zheng, Z., & Zehavi, I. 2005, *ApJ*, **631**, 41  
 Tully, R. B., & Fisher, J. R. 1977, *A&A*, **54**, 661  
 van de Voort, F., Springel, V., Mandelker, N., van den Bosch, F. C., & Pakmor, R. 2019, *MNRAS*, **482**, L85  
 Villaescusa-Navarro, F., Genel, S., Castorina, E., et al. 2018, *ApJ*, **866**, 135

Villaescusa-Navarro, F., Hahn, C., Massara, E., et al. 2020, *ApJS*, **250**, 2

Virtanen, P., Gommers, R., Oliphant, T. E., et al. 2020, *NatMe*, **17**, 261

Weigel, A. K., Schawinski, K., & Bruderer, C. 2016, *MNRAS*, **459**, 2150

Yamamoto, K., Nakamichi, M., Kamino, A., Bassett, B. A., & Nishioka, H. 2006, *PASJ*, **58**, 93

Yang, X., Mo, H. J., & van den Bosch, F. C. 2003, *MNRAS*, **339**, 1057

Zheng, Z. 2004, *ApJ*, **610**, 61

Zheng, Z., Coil, A. L., & Zehavi, I. 2007, *ApJ*, **667**, 760

Zheng, Z., & Guo, H. 2016, *MNRAS*, **458**, 4015

Zheng, Z., & Weinberg, D. H. 2007, *ApJ*, **659**, 1

Zwaan, M. A., Meyer, M. J., Staveley-Smith, L., & Webster, R. L. 2005, *MNRAS*, **359**, L30

Zwaan, M. A., Staveley-Smith, L., Koribalski, B. S., et al. 2003, *AJ*, **125**, 2842